JAAS

ROYAL SOCIETY OF CHEMISTRY

PAPER

Published on 27 January 2026
Licence and permissions

Cite this: *J. Anal. At. Spectrom.*, 2026, **41**, 1112

Quantitative analysis of fluorine and chlorine in apatite by femtosecond laser induced breakdown spectroscopy

Yunpeng Guo,[abc] Wubin Yang, *[ab] Shuang Yan,[ab] Zhenli Gao,[ac] Hecai Niu,[ab] Jhanis J. Gonzalez,[de] Chunyi Liu[d] and Richard E. Russo[de]

Received 20th October 2025
Accepted 26th January 2026

DOI: 10.1039/d5ja00404g

rsc.li/jaas

Halogens, including fluorine (F) and chlorine (Cl), play essential roles in magmatic, hydrothermal, and ore-forming processes. Determining their geochemical behaviors is challenging due to their low abundance and volatility. Apatite containing halogens serves as an ideal recorder of Earth's and planetary processes. This study presents a quantitative method using molecular emission spectra of calcium fluoride (CaF) and calcium chloride (CaCl) to measure F and Cl concentrations in apatite through femtosecond laser-induced breakdown spectroscopy (fs-LIBS). Reference materials with varying F and Cl levels were employed to optimize conditions and develop calibration curves for F (0.55–3.75 wt%) and Cl (0.45–4.26 wt%), with detection limits of 0.22 wt% and 0.38 wt%, respectively. The calibration curves achieved R^2 values of 0.995 for F and 0.992 for Cl, with RMSRE of 8% for F and 13% for Cl. Validation using natural apatite samples confirmed accuracy within ± 0.10 wt% compared to EPMA data. The fs-LIBS technique offers potential for accurate and precise measurement of F and Cl in minerals when reference materials are available.

1 Introduction

Fluorine (F) and chlorine (Cl), the most abundant halogen elements on Earth, are key volatile components released from magma, along with water, carbon dioxide, and sulfur.[1–3] Although present in low concentrations in magma, they significantly influence the physical properties of the magma system, such as viscosity, density, and solidus temperature.[4,5] Furthermore, they act as primary anion ligands in certain hydrothermal fluids, increasing the solubility and mobility of ore-forming metals and aiding their transport within hydrothermal systems.[6–8] Previous research shows that chlorine is more incompatible than fluorine, leading to chlorine preferentially partitioning into fluids while fluorine remains in the melt.[3,8,9] Thus, the concentrations and ratios of F and Cl serve as valuable geochemical tracers for understanding the physicochemical processes of magmatic and hydrothermal systems.[10–12] However, directly measuring their levels in these systems is challenging due to their low abundance and high volatility. Apatite [$Ca_5(PO_4)_3$(F, Cl, OH)] can incorporate specific proportions of halogen components into its unique crystal structure, making it an effective recorder of magmatic and hydrothermal systems,[12–14] as well as related ore-forming processes.[15–17]

An electron probe micro-analyzer (EPMA) is commonly employed for *in situ* analysis of F and Cl contents in apatite.[18,19] However, previous research indicates that the accuracy and precision of these measurements are significantly influenced by factors such as operating conditions, crystallographic orientation, the physicochemical properties of minerals, and alterations induced by electron beam interaction.[20,21] Furthermore, secondary ion mass spectrometry (SIMS) is recognized as a reliable technique for *in situ* halogen detection, yet its high costs and time-consuming protocols limit its broad application.[22,23] Other *in situ* methods for halogen analysis, such as proton-induced X-ray emission (PIXE)[24] and laser ablation inductively coupled plasma mass spectrometry (LA-ICP-MS),[25,26] fail to meet the requirements for routine simultaneous quantification of F and Cl.

Laser-Induced Breakdown Spectroscopy (LIBS) is a well-established *in situ* element analysis technique that enables the quantification of halogen concentrations by examining plasma emissions produced through laser interactions with the sample surface.[27] LIBS offers notable benefits, including high spatial resolution, rapid analysis times, and minimal sample preparation requirements. Elements are identified by their optical emission lines, with the resulting spectrum serving as the

[a]*State Key Laboratory for Deep Earth Processes and Resources, Guangzhou Institute of Geochemistry, Chinese Academy of Sciences, Guangzhou 510640, China. E-mail: yangwubin@gig.ac.cn*

[b]*Guangdong Research Center for Strategic Metals and Green Utilization/Guangdong Provincial Key Laboratory of Mineral Physics and Materials, Guangzhou Institute of Geochemistry, Chinese Academy of Sciences, Guangzhou 510640, China*

[c]*University of Chinese Academy of Sciences, Beijing, China*

[d]*Applied Spectra, 950 Riverside Pkwy Suite 90, West Sacramento, CA 95605, USA*

[e]*Lawrence Berkeley National Laboratory, Berkeley, CA 94720, USA*

chemical fingerprint of samples. For most halogens, the strongest emission lines are in the ultraviolet (UV) range (<200 nm) of the spectrum. However, detecting these lines requires a specialized UV-sensitive spectrometer operated under vacuum to avoid absorption by atmospheric species.[28,29] Alternatively, other emissions appear in the visible and near-infrared regions, such as 685.6 nm for F(I) and 837.6 nm for Cl(I).[30,31] Nevertheless, these line intensities are typically too weak for analyzing low concentrations due to their high excitation energy levels.[32–34] Some alternative methods can assist in detecting these halogens. For example, molecular emissions from species such as CaF and CaCl have been used as proxies for F and Cl detection in various matrices. For example, Gaft *et al.* (2014) utilized CaF and CaCl molecular emissions, noting that these are considerably more sensitive under ambient conditions than atomic lines.[33] Later, Forni *et al.* (2015), working with data from the ChemCam instrument on the Curiosity rover, employed CaF and CaCl emissions to detect F and Cl.[35] Vogt *et al.* (2020) analyzed these emissions under simulated Martian atmospheric conditions, achieving detection limits of 0.4 wt% for F and 1.8 wt% for Cl.[36] Recently, Quarles *et al.* (2025) used the CaF molecular emission around 603 nm to quantify the F contents in apatite, with an absolute error within 0.1%.[37] CaF and CaCl molecular emissions have also been used to detect F and Cl in ores, cement, biological apatite, and calcium-free samples by nebulizing calcium-containing solutions onto the sample surfaces.[38–44] However, the precise simultaneous quantification of F and Cl in calcium-rich minerals, such as apatite, remains challenging. Femtosecond laser-induced breakdown spectroscopy (fs-LIBS) offers significant advantages for analyzing apatite, particularly due to the ultrashort duration of the laser pulses. The femtosecond-scale pulse duration minimizes thermal effects during ablation, resulting in reduced melting and collateral damage to the samples.[45,46] The low thermal impact also allows for repeated measurements on the same sample area or adjacent regions without compromising structural integrity, enabling more extensive and high-resolution spatial analysis. This precision is particularly beneficial when studying apatite, which often contains delicate compositional zoning or inclusions that are easily altered by thermal effects.

This study examined the use of CaF and CaCl molecular emission spectra to determine F and Cl concentrations in apatite *via* fs-LIBS. We systematically evaluated the impact of various gaseous environments (air, He, and Ar), gate delay, and gate width on the intensity of CaF and CaCl emissions. Calibration curves were then developed to relate CaF and CaCl emissions to F and Cl concentrations in apatite. Finally, this method was applied to simultaneously measure F and Cl concentrations in natural apatite samples.

2 Experimental

2.1 Samples

In this study, nine apatite reference materials were analyzed, and their reference values are summarized in Table 1. Five apatite samples, including TUBAF#38, TUBAF#40, TUBAF#50, MGMH#128441A, and Apatite MZ-TH, were obtained from IAGeo Limited in the United Kingdom.[47,48] Four additional apatite reference materials, such as Durango, MAD, McClure, and Morocco, were reported in previous studies.[49,50] The calibration curve for F was established using the integrated CaF signals of TUBAF#38, TUBAF#40, MGMH#128441A and MAD. Meanwhile, the calibration curve for Cl was developed using the integrated CaCl signals of Durango, TUBAF#38, TUBAF#40, and MGMH#128441A.

Table 1 F and Cl contents (wt%) and standard deviations (1SD) of the natural apatite reference materials in this study[a]

	By EPMA		By fsLIBS	
Sample	F contents	Cl contents	F contents	Cl contents
TUBAF#40	1.79 ± 0.07	1.34 ± 0.03	1.78 ± 0.06	1.32 ± 0.07
TUBAF#38	0.55 ± 0.06	4.26 ± 0.10	0.51 ± 0.02	4.27 ± 0.09
Durango	3.09 ± 0.03	0.45 ± 0.01	3.11 ± 0.06	0.49 ± 0.06
MGMH#128441A	2.26 ± 0.10	0.94 ± 0.04	2.32 ± 0.08	0.96 ± 0.06
TUBAF#50	3.29 ± 0.12	0.50 ± 0.02	3.27 ± 0.08	0.50 ± 0.04
Apatite MZ-TH	3.60 ± 0.15	bdl	3.57 ± 0.07	bdl
MAD	3.75 ± 0.08	0.25 ± 0.02	3.66 ± 0.08	bdl
McClure	3.38 ± 0.21	bdl	3.34 ± 0.08	bdl
Apatite Morocco	2.41 ± 0.22	0.78 ± 0.10	2.47 ± 0.06	0.73 ± 0.07

[a] Data labeled with 'bdl' were below detection limit.

2.2 EPMA analysis

EPMA was conducted on a JEOL JXA 8230 electron microprobe at Guangzhou Institute of Geochemistry, Chinese Academy of Sciences (GIGCAS). Representative apatite grains were hand-picked under a binocular microscope, mounted in epoxy, and polished to approximately half the thickness for further analysis. The analytical conditions for EPMA of apatite were as follows: 15 kV accelerating voltage, 10 nA beam current, and 5 μm beam diameter. The analytical results were reduced using ZAF correction. The used standards were fluorapatite for Ca and P, BaF_2 for F, tugtupite for Cl. The relative precisions were ± 2% for Ca, P and F and ± 5% for Cl.

2.3 LIBS analysis and data processing

LIBS analysis was conducted using a J200 Tandem QX femtosecond LA/LIBS system from Applied Spectra Inc. at GIGCAS. This instrument features a 343 nm femtosecond laser with a variable repetition rate of 1 to 10 kHz, along with adjustable energy and ablation spot size. After each laser pulse, the emitted radiation was collected through a high-transmission fiber optic cable to maximize the collection of plasma light. The collected light was then analyzed with a Czerny–Turner spectrometer paired with a high-performance ICCD detector equipped with a dual-grating turret (2400 g mm^{-1} for UV or 1200 g mm^{-1} for visible and NIR coverage). Optimized LIBS parameters, including gate delay (the interval between the laser pulse and data acquisition start), gate width (duration of data acquisition), laser energy, and the ambient gas used in the chamber, were applied. LIBS data were visualized and processed using Axiom-EX software provided by the manufacturer, which records the spectrum from the spectrometers for each laser

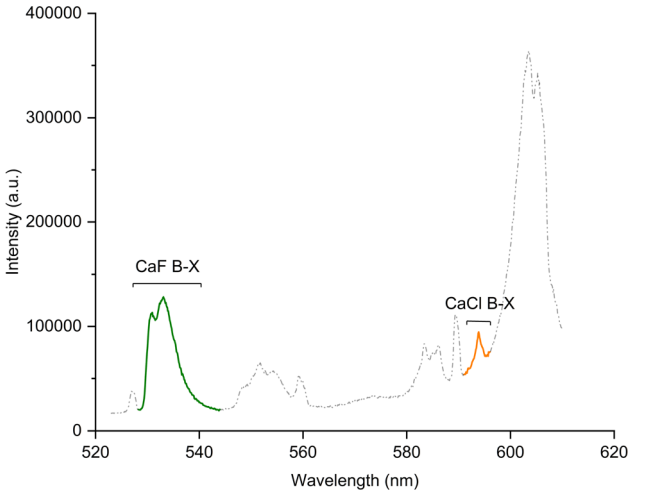

Fig. 1 fsLIBS spectrum of natural apatite (MGMH#128441A), with B–X bands at 529–545 nm for CaF (green) and at 590–596 nm for CaCl (orange). The spectra were obtained using a femtosecond laser at 343 nm, with a 40 μm spot size, 90 μJ pulse energy, and an argon flow rate of 1.0 L min^{-1}.

shot. During analysis, we selected a wavelength range of 518 nm to 618 nm for ICCD detection, allowing for the simultaneous acquisition of CaF (B–X) and CaCl (B–X) molecular emissions, as shown in Fig. 1. The laser spot size was set to 40 μm with an energy of 90 μJ. We evaluated ten raster lines, each 0.05 mm long, across each apatite reference material. Each raster line included 25 individual shots (emission spectra), which were then summed. The operating conditions are summarized in Table 2.

Data processing to obtain CaF and CaCl integrated signals followed the procedures previously published by Mendez-Lopez *et al.*[51] The data processing involved four steps. First, raw spectra were normalized to a calcium oxide emission region. Second, a mean blank spectrum was calculated and subtracted from each spectrum to eliminate interfering signals. Third, polynomial fitting was employed to correct for atomic interferences. Finally, the baseline was adjusted, and emission intensities were integrated within the designated spectral ranges. All the data processing procedures were completed using Python 3.13. It should be noted that CaCl molecular emission spans various spectral ranges depending on Cl concentrations.[52] When calculating the integrated net area of the CaCl molecular emission within the same range, samples with low Cl concentrations are significantly affected by background noise. Therefore, we used a variable integration range where the CaCl emission intensity exceeds 5% of its maximum value at 593.5 nm to determine the integrated net area of the CaCl molecular emission.

Table 2 Operating conditions for fsLIBS used in this study

Laser probe	
Laser wavelength (nm)	343
Pulse width (fs)	400
Pulse energy (μJ)	90
Repetition rate (Hz)	8
Scan speed (μm s^{-1})	200
Line length (μm)	50
Spectroscopy	
Spectral detector	ICCD
Plasma gas ambient	Argon
Grating (g mm^{-1})	1200
Gate delay (μs)	1.2
Gate width (μs)	2.5
Wavelength range (nm)	523–610

3 Results and discussion

3.1 Gaseous environment and temporal optimization

Apatite sample MGMH#128441A was used to determine the optimal conditions in this study. Previous research has documented that introducing a noble gas into the plasma generation environment can change plasma characteristics, such as excitation temperatures and electron densities, which in turn affects the intensity of molecular emissions.[53] Most of these studies investigated the impact of gaseous environments on CaF and CaCl molecular emissions from substrates such as teeth and cement using nanosecond LIBS.[42,52] However, the differences in ablation mechanisms between femtosecond and nanosecond LIBS due to pulse duration mean that ns-LIBS results cannot be directly applied to fs-LIBS. Furthermore, the effect of using a 343 nm femtosecond laser and different gaseous environments on the CaF and CaCl molecular signals from an apatite substrate has not been studied. To address this, the influence of three gaseous environments (*i.e.*, argon, air, and helium) on CaF and CaCl molecular emissions was investigated under consistent temporal conditions using fs-LIBS. Our results showed that both the intensity and stability of CaF and CaCl molecular emissions increased notably in an argon atmosphere compared to air and helium. In contrast, only weak and inconsistent emissions were observed in a helium atmosphere. Thus, argon was selected as the environmental gas for quantitative analysis in this study.

The impact of varying timing conditions, specifically gate delay and gate width, on CaF and CaCl molecular emissions was also assessed. A variable gate delay ranging from 0.8 μs to 2.0 μs was tested with a fixed gate width of 2.5 μs, as shown in Fig. 2. Our results showed that both CaF and CaCl signal intensities decreased as gate delay increased from 0.8 μs to 2.0 μs, albeit with slightly differing decay patterns. CaCl signal intensity dropped sharply between 1.2 and 1.4 μs before stabilizing into a steady decline, while CaF signal intensity decreased consistently across the entire measured range from 0.8 to 2.0 μs. Notably, there is less overlap from Ca and Na atomic emission in both CaF and CaCl regions at 1.2 μs gate delay than before, particularly between Ca(I) atomic emission and CaF molecular emission, as shown in Fig. 2b. This overlap would have caused significant analytical errors for quantification of F and Cl in

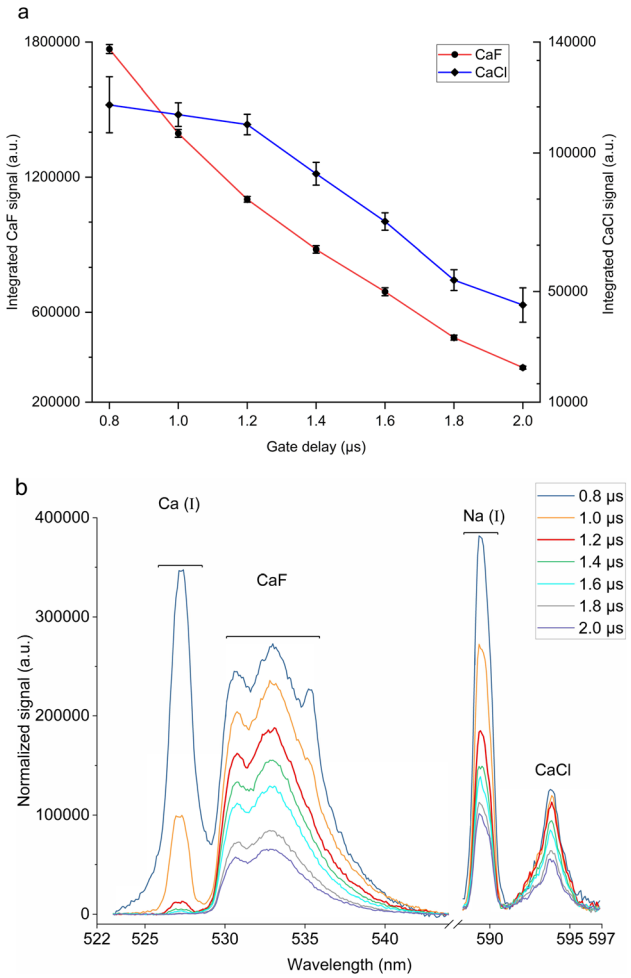

Fig. 2 Molecular emission intensity of CaF and CaCl at varying gate delays, with a constant gate width of 2.5 μs. The error bar is the standard deviations (SD) of ten replicated ablated raster lines. (a) Integrated intensity of CaF and CaCl emissions at different gate delays. (b) LIBS spectra of CaF and CaCl emissions at different gate delays.

apatite. Therefore, a gate delay of 1.2 μs was selected as an optimal balance, maintaining adequate molecular signal intensity while minimizing atomic line interference.

Gate widths from 0.5 μs to 5.0 μs were also evaluated with a constant gate delay of 1.2 μs, as shown in Fig. 3. Our results indicated that the emission intensity of CaF and CaCl molecules increased with gate width, reaching a maximum plateau at around 3.5 μs. It is obvious that the intensities of integrated CaF and CaCl signals are strong enough for subsequent analysis from 2.5 μs to 3.5 μs. Additionally, the error bar (1SD) of CaF and CaCl signals was relatively shorter at 2.5 μs gate width than other gate widths, especially for the CaF signal. This observation suggested that the repeatability of CaF and CaCl integrated signals was relatively greater at 2.5 μs. Consequently, a gate width of 2.5 μs was selected as the optimal compromise, providing sufficient signal intensity accumulation with reliable statistical repeatability. In summary, the optimal timing conditions for this study were determined to be a 1.2 μs gate delay combined with a 2.5 μs gate width.

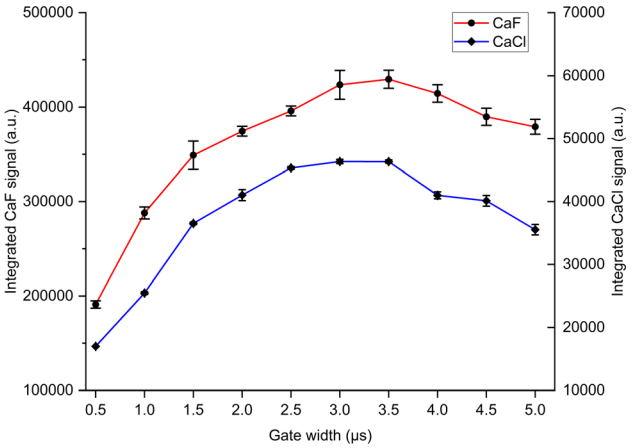

Fig. 3 Integrated CaF and CaCl signals at varying gate widths, with a constant gate delay of 1.2 μs. The error bar is the standard deviations (SD) of ten replicated ablated raster lines.

3.2 Univariate calibration procedures

Under optimized conditions, a series of apatite samples with increasing F and Cl contents were selected to establish univariate calibration curves relating the integrated CaF and CaCl signals to F and Cl concentrations, as detailed in Fig. 4. The uncertainty of each data point is represented by the standard deviation (SD) of the 10 CaCl and CaF integrated signals obtained from each sample. The determination coefficient (R^2) represents analytical linearity. The SD of the 10 integrated background values (σ_B) and the slope of the calibration curve (k) were used to calculate the limits of detection (LOD) using the $3\sigma_B$ criterion,[54] as shown in Fig. 4, with the following equation:

$$\mathrm{LOD} = \frac{3\sigma_B}{k}$$

Additionally, to verify these results and account for the limited number of calibration samples, a Leave-One-Out Cross-Validation (LOOCV) procedure was performed. In this approach, one sample removed from the calibration set and then tested with the remaining samples and a blank. Four calibration curves were generated, and for each, the concentration of the excluded sample was calculated using the calibration curve derived from the other three samples and a blank. The Root Mean Square Relative Error (RMSRE) was used as the evaluation metric for LOOCV and is defined by the equation below:

$$\mathrm{RMSRE}(\%) = \sqrt{\frac{1}{N}\sum\left(\frac{x_i - x_0}{x_0}\right)^2} \times 100\%$$

where N is the number of iterations, x_i is the concentration calculated from the calibration curve, and x_0 is the nominal concentration value.

The R^2 and LOD values for the univariate calibration curves reported in this study were 0.995 and 0.22 wt% for F, and 0.992 and 0.38 wt% for Cl. The RMSRE of the univariate calibration curves were 8% for F and 13% for Cl.

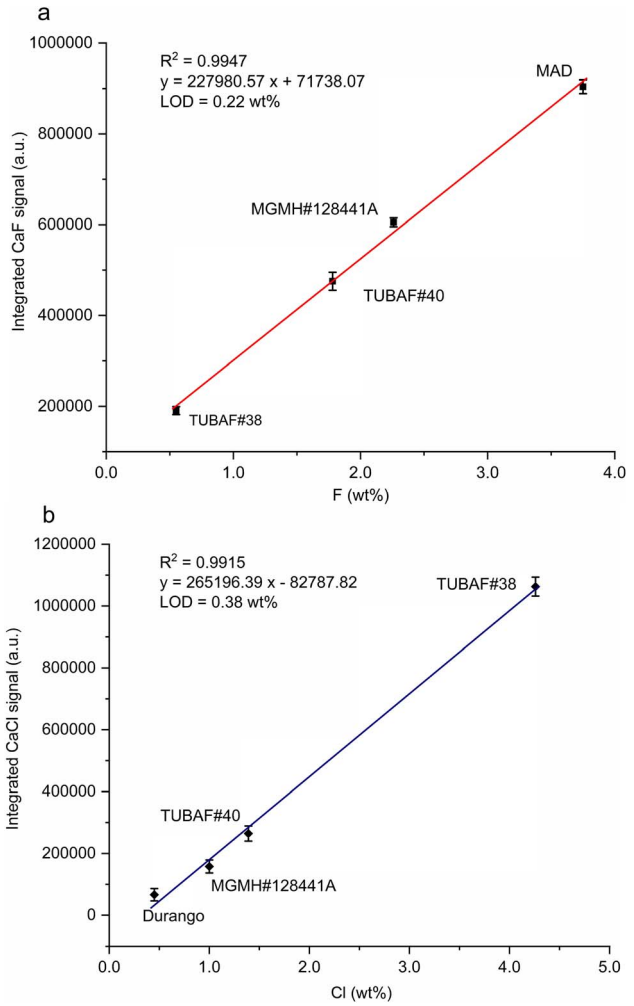

Fig. 4 Calibration curve showing the relationship between integrated CaF signals with F contents (a) and integrated CaCl signals with Cl contents (b) in apatite reference materials.

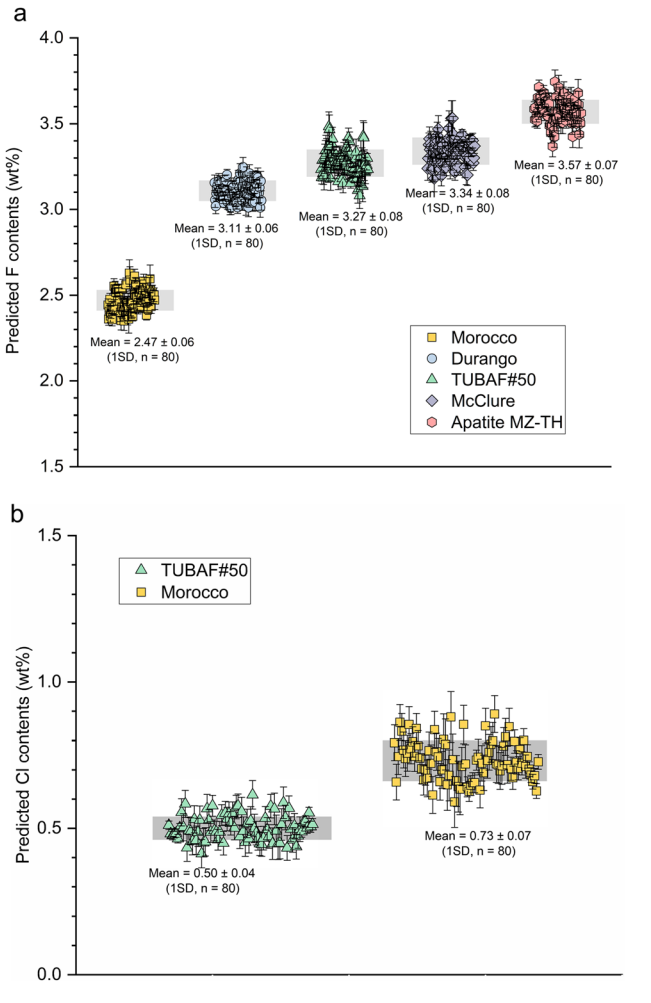

Fig. 5 Predicted F (a) and Cl (b) contents, along with their standard deviations, in natural apatite samples using fsLIBS by univariate analytical calibration methods in this study.

3.3 Applications

To verify the accuracy, precision, and repeatability of the univariate calibration curves mentioned above, a comprehensive set of measurements was conducted using various apatite reference materials under optimal experimental conditions. Five natural apatite samples (*i.e.*, McClure, TUBAF#50, Durango, Morocco, and Apatite MZ-TH) were selected to test the F calibration curve, while two apatite samples (*i.e.*, TUBAF#50 and Morocco) were used for the Cl calibration curve. Each reference material underwent eighty replicate ablated raster lines to ensure statistical robustness. The F and Cl contents in these samples were calculated based on the predicted concentrations from the fit line equations established during calibration. Since no widely accepted reference values for F and Cl in apatite exist from other standardized methods, EPMA results for these reference materials served as the comparative standards for evaluating the accuracy and precision of our LIBS measurements.

The predicted F contents for Morocco, Durango, TUBAF#50, McClure, and Apatite MZ-TH were 2.47 ± 0.06 wt%, 3.11 ± 0.06 wt%, 3.27 ± 0.08 wt%, 3.34 ± 0.08 wt%, and 3.57 ± 0.07 wt%, respectively, with all values expressed within one standard deviation. The predicted Cl contents were 0.50 ± 0.04 wt% for TUBAF#50 and 0.73 ± 0.07 wt% for Morocco, as shown in Fig. 5. Additional samples, including TUBAF#38, TUBAF#40, MGMH#128441A, and MAD, were designated as F monitor samples, while Durango, TUBAF#38, TUBAF#40, and MGMH#128441A served as Cl monitor samples. Each of these monitor samples was tested in fifty replicate raster lines. The recalculated F contents from these measurements were 0.51 ± 0.02 wt% (TUBAF#38), 1.78 ± 0.06 wt% (TUBAF#40), 2.32 ± 0.08 wt% (MGMH#128441A), and 3.66 ± 0.08 wt% (MAD). For Cl, the contents were 0.49 ± 0.06 wt% (Durango), 4.27 ± 0.09 wt% (TUBAF#38), 1.32 ± 0.07 wt% (TUBAF#40), and 0.96 ± 0.06 wt% (MGMH#128441A). All LIBS and EPMA data are plotted in Fig. 6, demonstrating that LIBS measurements generally align with EPMA results within error margins, with replicate experiment errors for both F and Cl concentrations being less than 0.10 wt%. This consistency affirms that, although LIBS can achieve accuracy comparable to EPMA, sample variability and spectral fluctuations can slightly affect measurement precision.

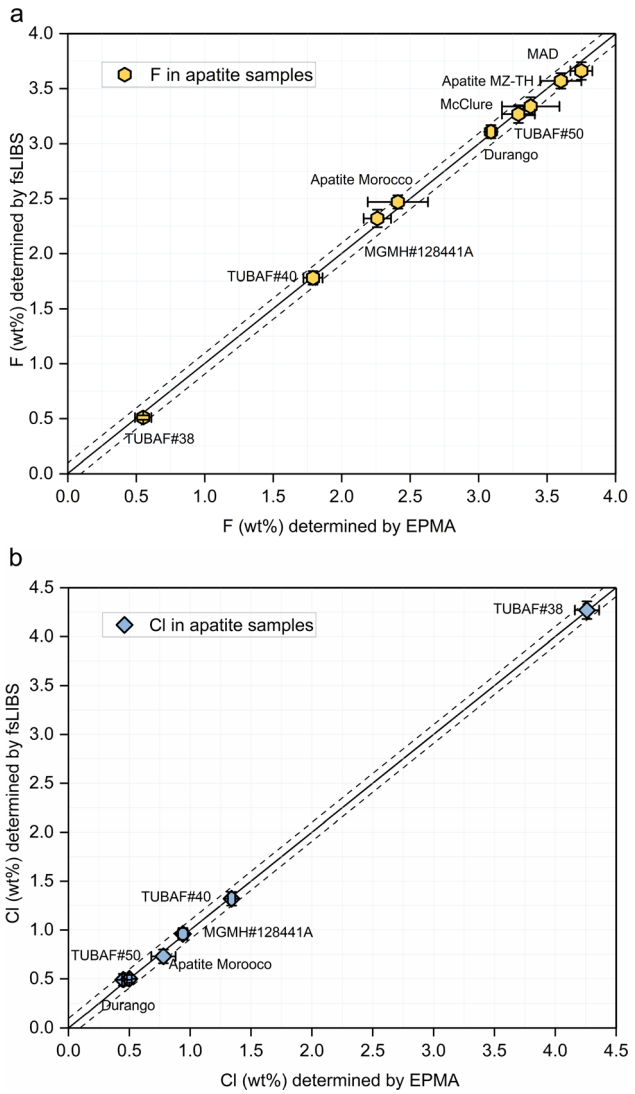

Fig. 6 Comparison of F (a) and Cl (b) contents in apatite determined by fsLIBS and EPMA. The solid lines are 1 : 1 line. The dotted lines denote uncertainly of ±0.1 wt% for both F and Cl contents.

4 Conclusions

This study demonstrated the use of proxy signals for accurate and precise quantification of F and Cl in apatite, a challenge for other techniques for many years. By leveraging CaF and CaCl molecular emissions in femtosecond laser-induced breakdown spectroscopy (fs-LIBS), this work provides a new approach for reliable halogen analysis in geological materials. First, the influence of different gaseous environments (air, He, and Ar) and temporal conditions (gate delay time and gate width) on the molecular emission of CaF and CaCl was evaluated using a 343 nm femtosecond laser. Our results indicated that the gas environment significantly affects these emissions, with Ar gas enhancing both intensity and stability. A significant advantage of fs-LIBS is its ultrashort pulse duration, which minimizes thermal effects and enables multiple analyses on the same sample without compromising integrity or altering composition. This capability facilitates dense spatial sampling and improves statistical reliability, particularly for heterogeneous materials such as apatite. Subsequently, quantitative analysis of F and Cl contents in natural apatite was performed using CaF and CaCl molecular bands with univariate calibration curves. To validate this method, we measured F and Cl contents in a set of natural apatite reference materials. Our fs-LIBS results aligned well with EPMA measurements within error, with absolute errors for replicate experiments of F and Cl concentrations in verification samples being less than 0.10 wt%. While fs-LIBS generally matches the accuracy of EPMA, instrument variability and spectral fluctuations may slightly reduce repeatability. Nonetheless, the strong agreement between fs-LIBS and EPMA data confirms the reliability and potential of this femtosecond-based approach for apatite studies.

Conflicts of interest

There are no conflicts to declare.

Data availability

The data supporting this article have been included as part of the supplementary information (SI). Supplementary information is available. See DOI: https://doi.org/10.1039/d5ja00404g.

Acknowledgements

We are grateful to the Science editor and three anonymous reviewers for their insightful comments. This work was financially supported by the Strategic Priority Research Program of the Chinese Academy of Sciences (XDA0430203), National Key Research and Development Program of China (2021YFC2901705), and Guangdong Science and Technology Program (2024B0303390002).

References

1 M. Alletti, D. R. Baker, B. Scaillet, A. Aiuppa, R. Moretti and L. Ottolini, *Chem. Geol.*, 2009, **263**, 37–50.
2 T. P. Fischer, *Geochem. J.*, 2008, **42**, 21–38.
3 M. A. Kendrick, *Annu. Rev. Earth Planet. Sci.*, 2024, **52**, 195–220.
4 A. Baasner, B. Schmidt and S. L. Webb, *Chem. Geol.*, 2013, **357**, 134–149.
5 J. Filiberto and A. H. Treiman, *Chem. Geol.*, 2009, **263**, 60–68.
6 Y. Wang, Q. Wang, D. I. Groves, S. Xue, T. Wang, L. Yang and J. Deng, *Geochim. Cosmochim. Acta*, 2024, **376**, 1–13.
7 A. A. Migdisov and A. Williams-Jones, *Miner. Deposita*, 2014, **49**, 987–997.
8 P. Lecumberri-Sanchez and R. J. Bodnar, *The Role of Halogens in Terrestrial and Extraterrestrial Geochemical Processes: Surface, Crust, and Mantle*, 2018, 261–305.
9 H. G. Eggenkamp, M. A. Marks, P. Atanasova, T. Wenzel and G. Markl, *Minerals*, 2020, **10**, 995.

10 P. M. Piccoli and P. A. Candela, *Rev. Mineral. Geochem.*, 2002, **48**, 255–292.
11 P. Lecumberri-Sanchez and R. J. Bodnar, in *The Role of Halogens in Terrestrial and Extraterrestrial Geochemical Processes: Surface, Crust, and Mantle*, Springer, 2018, pp. 261–305.
12 J. D. Webster, B. A. Goldoff, R. N. Flesch, P. A. Nadeau and Z. W. Silbert, *Am. Mineral.*, 2017, **102**, 61–74.
13 J. D. Webster and P. M. Piccoli, *Elements*, 2015, **11**, 177–182.
14 P. Qu, W. Yang, H. Niu, N. Li and D. Wu, *GSA Bulletin*, 2022, **134**, 1863–1876.
15 J. M. Pedersen, T. Ulrich, M. J. Whitehouse, A. J. Kent and C. Tegner, *Contrib. Mineral. Petrol.*, 2021, **176**, 102.
16 M. A. Marks, T. Wenzel, M. J. Whitehouse, M. Loose, T. Zack, M. Barth, L. Worgard, V. Krasz, G. N. Eby and H. Stosnach, *Chem. Geol.*, 2012, **291**, 241–255.
17 B. A. Konecke, A. Fiege, A. C. Simon and F. Holtz, *Geology*, 2017, **45**, 739–742.
18 D. Zhang, Y. Chen, B. Su, C. Qi and Q. Mao, *Prog. Earth Planet. Sci.*, 2023, **10**, 29.
19 S. Flemetakis, J. Berndt, S. Klemme, F. Genske, A. Cadoux, M. Louvel and A. Rohrbach, *Microsc. Microanal.*, 2020, **26**, 857–866.
20 M. J. Stock, M. C. Humphreys, V. C. Smith, R. D. Johnson and D. M. Pyle, *Am. Mineral.*, 2015, **100**, 281–293.
21 B. Goldoff, J. D. Webster and D. E. Harlov, *Am. Mineral.*, 2012, **97**, 1103–1115.
22 Y. Chen, J. Gao, X. Bi, S. Dong, Q. Lei and R. Hu, *J. Anal. At. Spectrom.*, 2024, **39**, 3000–3009.
23 Y. Liu, Q. Li, G. Tang and X. Li, *Crystals*, 2022, **12**, 383.
24 H. élène Bureau and N. Métrich, *Geochim. Cosmochim. Acta*, 2003, **67**, 1689–1697.
25 J. Hammerli, B. Rusk, C. Spandler, P. Emsbo and N. H. Oliver, *Chem. Geol.*, 2013, **337**, 75–87.
26 J. H. Seo, M. Guillong, M. Aerts, Z. Zajacz and C. A. Heinrich, *Chem. Geol.*, 2011, **284**, 35–44.
27 P. K. Diwakar, K. H. Loper, A.-M. Matiaske and D. W. Hahn, *J. Anal. At. Spectrom.*, 2012, **27**, 1110.
28 N. Omenetto, W. Jones, B. Smith, T. Guenther and E. Ewusi-Annan, *Research Final Report*, University of Florida - Department of Chemistry, 2016.
29 P. Pořízka, S. Kaski, A. Hrdlička, P. Modlitbová, L. Sládková, H. Häkkänen, D. Prochazka, J. Novotný, P. Gadas and L. Čelko, *J. Anal. At. Spectrom.*, 2017, **32**, 1966–1974.
30 C. D. Quarles, J. J. Gonzalez, L. J. East, J. H. Yoo, M. Morey and R. E. Russo, *J. Anal. At. Spectrom.*, 2014, **29**, 1238–1242.
31 A. de Pablos-Martín, A. T. Contreras Jaimes, S. Wahl, S. Meyer and D. S. Brauer, *Int. J. Appl. Glass Sci.*, 2021, **12**, 213–221.
32 D. Vogt, K. Rammelkamp, S. Schröder and H.-W. Hübers, *Icarus*, 2018, **302**, 470–482.
33 M. Gaft, L. Nagli, N. Eliezer, Y. Groisman and O. Forni, *Spectrochim. Acta, Part B*, 2014, **98**, 39–47.
34 P. A. Mello, J. S. Barin, F. A. Duarte, C. A. Bizzi, L. O. Diehl, E. I. Muller and E. M. Flores, *Anal. Bioanal. Chem.*, 2013, **405**, 7615–7642.
35 O. Forni, M. Gaft, M. J. Toplis, S. M. Clegg, S. Maurice, R. C. Wiens, N. Mangold, O. Gasnault, V. Sautter and S. Le Mouélic, *Geophys. Res. Lett.*, 2015, **42**, 1020–1028.
36 E. Clavé, D. Vogt, S. Schröder, S. Maurice and B. Bousquet, *Spectrochim. Acta, Part B*, 2022, **194**, 106464.
37 C. D. Quarles Jr, B. T. Manard, N. A. Zirakparvar, J. Petrus, B. Paul, D. Douglas, A. Gleadow, B. Kohn, S. Boone and L. Chung, *Geostand. Geoanal. Res.*, 2025, DOI: 10.1111/ggr.70021.
38 C. Alvarez-Llamas, J. Pisonero and N. Bordel, *Spectrochim. Acta, Part B*, 2016, **123**, 157–162.
39 B. T. Manard, C. J. Hintz, C. D. Quarles Jr, W. Burns, N. A. Zirakparvar, D. R. Dunlap, T. Beiswenger, A. M. Cruz-Uribe, J. A. Petrus and C. R. Hexel, *Metallomics*, 2022, **14**, 6631561.
40 T. Dietz, C. Gottlieb, P. Kohns and G. Ankerhold, *Spectrochim. Acta, Part B*, 2019, **161**, 105707.
41 Z. Tang, R. Zhou, K. Liu, Z. Hao, K. Liu, W. Zhang, Q. Li, C. Zhu and X. Li, *J. Anal. At. Spectrom.*, 2021, **36**, 1735–1741.
42 M. Martinez, G. J. Harry, E. N. Haynes, P.-I. Lin, E. Oken, M. K. Horton, R. O. Wright, M. Arora and C. Austin, *J. Anal. At. Spectrom.*, 2023, **38**, 303–314.
43 C. Alvarez-Llamas, J. Pisonero and N. Bordel, *J. Anal. At. Spectrom.*, 2017, **32**, 162–166.
44 Z. Tang, Z. Hao, R. Zhou, Q. Li, K. Liu, W. Zhang, J. Yan, K. Wei and X. Li, *Talanta*, 2021, **224**, 121784.
45 V. Margetic, A. Pakulev, A. Stockhaus, M. Bolshov, K. Niemax and R. Hergenröder, *Spectrochim. Acta, Part B*, 2000, **55**, 1771–1785.
46 F. J. Fortes, J. Moros, P. Lucena, L. M. Cabalín and J. J. Laserna, *Anal. Chem.*, 2013, **85**, 640–669.
47 A. Wudarska, E. Słaby, M. Wiedenbeck, J. D. Barnes, M. Bonifacie, N. C. Sturchio, G. Bardoux, F. Couffignal, J. Glodny and L. Heraty, *Geostand. Geoanal. Res.*, 2021, **45**, 121–142.
48 A. Wudarska, M. Wiedenbeck, E. Słaby, M. Lempart-Drozd, C. Harris, M. M. Joachimski, C. Lécuyer, K. G. MacLeod, A. Pack and T. Vennemann, *Geostand. Geoanal. Res.*, 2022, **46**, 277–306.
49 Y.-H. Yang, F.-Y. Wu, J.-H. Yang, D. M. Chew, L.-W. Xie, Z.-Y. Chu, Y.-B. Zhang and C. Huang, *Chem. Geol.*, 2014, **385**, 35–55.
50 F. E. Apen, C. J. Wall, J. M. Cottle, M. D. Schmitz, A. R. Kylander-Clark and G. G. Seward, *Chem. Geol.*, 2022, **590**, 120689.
51 C. Mendez-Lopez, L. J. Fernandez-Menendez, C. Gonzalez-Gago, J. Pisonero and N. Bordel, *Opt Laser. Technol.*, 2023, **164**, 109536.
52 L. J. Fernández-Menéndez, C. Méndez-López, C. González-Gago, J. Pisonero and N. Bordel, *J. Anal. At. Spectrom.*, 2023, **38**, 325–332.
53 J. A. Aguilera and C. Aragón, *Appl. Phys. A: Mater. Sci. Process.*, 1999, **69**, S475–S478.
54 J.-M. Mermet, *Spectrochim. Acta, Part B*, 2008, **63**, 166–182.